Topological α-Sn surface states versus film thickness and strain

S. Küfner,* M. Fitzner, and F. Bechstedt

Institut für Festkörpertheorie und -optik, Friedrich-Schiller-Universität Jena, Max-Wien-Platz 1, 07743 Jena, Germany

(Received 23 July 2014; revised manuscript received 5 September 2014; published 22 September 2014)

The theoretical prediction that gray tin represents a strong topological insulator under strain [L. Fu and C.L. Kane, Phys. Rev. B **76**, 045302 (2007)] is proven for biaxially strained α-Sn layers with varying thickness by means of a generalized density functional theory with a nonlocal exchange-correlation potential that widely simulates quasiparticle bands and a tight-binding method including intra- and interatomic spin-orbit interaction. Hydrogen-passivated surfaces are modeled by symmetric slabs. In contrast to the conventional picture of a topological insulator, we find topological gapless surface states below the strain-induced bulk gap, in agreement with photoemission studies. The topological surfaces states do not emerge out of the lower Γ_8^+ states but are strongly influenced by the inverted bulk Γ_7^- band, i.e., lie within the negative bulk sp gap. We show that the position of the Dirac point and the dispersion of the surrounding bands depend on the thickness of the α-Sn layer but are less influenced by strain. The resulting Fermi velocities agree well with available photoemission data.

DOI: 10.1103/PhysRevB.90.125312 PACS number(s): 73.20.At, 75.70.Tj, 71.70.Fk, 73.43.Cd

I. INTRODUCTION

An attractive perspective for physical properties and applications in spintronics was opened up by the theoretical prediction [1–3] and experimental realization [4–6] of topological insulators (TIs) [7–9]. Three-dimensional (3D) TIs embody a topological nontrivial quantum state of matter where an insulating bulk with an inverted gap induced by a strong spin-orbit coupling (SOC) is necessarily accompanied by gapless states. These states bridge the bulk gap, are localized at the surface, and are protected by time-reversal symmetry. Therefore, they are frequently called surface states. However, to distinguish them from those due to the modifications of chemical bonding, e.g., dangling bonds, they are sometimes called edge states to underline the topological character. Here, we use the denotation topological surface states (TSSs) as a compromise to illustrate their character and their localization simultaneously. The TI phase was first demonstrated in two dimensions in HgTe/HgCdTe quantum wells [4] with the particular character of a quantum spin Hall (QSH) phase [2]. A recent analysis of the sequence of measured quantum Hall plateaus [10] suggested that a symmetry-lowering strain opens a gap in the zero-gap semiconductor (or semimetal) HgTe [11] so that the TI properties can be explored by tuning the Fermi energy into the "bulk" gap and probing the transport properties of the gapless topological states [12]. The strain in the HgTe layers grown biaxially by molecular beam epitaxy stems from a 0.23% lattice mismatch between HgTe and the CdTe substrate. It opens a small gap of about 15 meV between the light-hole and heavy-hole bands.

The topological effects are due to two unique properties of the band structure of the zinc-blende compound HgTe: (i) the fourfold degeneracy of the light-hole and heavy-hole Γ_8 bands at the Brillouin zone (BZ) center Γ and (ii) the energetic inversion of the $s_{1/2}$-type Γ_6 and $p_{3/2}$-type Γ_8 band ordering. Both properties distinguish HgTe from conventional zinc-blende semiconductors such as CdTe. Under strain, the first property leads to a 3D TI, while the second one is the origin of the QSH effect in 2D HgTe quantum wells. The diamond-structure crystal α-Sn possesses a very similar inverted band structure [13]. Indeed, very recently a 3D topological phase in strained α-Sn (001) films has been reported [14,15]. These films are pseudomorphically grown on InSb(001) substrates, so that they are biaxially strained. The slight compressive strain amounts to 0.14%. Thick and ultrathin layers with varying thicknesses 0.1 to 1 μm [14] and 2.0 to 5.5 nm [15], respectively, have been investigated. Angle-resolved photoemission spectroscopy (ARPES) including spin detection has been used to probe TSSs for ultrathin and thick α-Sn films.

The measurements have been interpreted by surface electronic structure calculations in the framework of the density functional theory (DFT) within a modified local density approximation (LDA) for exchange and correlation (XC) including SOC [14,15]. The calculations are however not straightforward. In order to obtain a correct energetic ordering of the bulk bands near Γ an empirical on-site Coulomb repulsion $U = 3.5$ eV [16] has to be added to the LDA XC functional for p states [14]. A modified Becke-Johnson (MBJ) potential together with the XC potential from LDA [17,18] also describes the correct ordering of the bulk bands and their energetic distances. However, the application of both approaches to surfaces is accompanied by some difficulties. The LDA+U method still tends to too low-lying L_6^- states, whereas the MBJLDA functional is not applicable for systems with large electron density gradients as such appearing in the transition between vacuum and α-tin. In contrast, the interface between HgTe and CdTe is treatable within the MBJLDA method because of the same MBJ parameters for both materials [19]. Nevertheless, the results of both theoretical methods confirm the observation of Dirac-cone-like surface-state bands with helical spin polarization. Thereby, their bulk origin and the energetic position of the Dirac point seem to depend on film thickness and substrate doping and are, therefore, under discussion.

In this paper, we study surfaces of biaxially strained α-Sn within two defined electronic structure methods including SOC. The thinner α-Sn films are investigated using the hybrid XC functional HSE06 containing a fraction of short-range

*Sebatian.Kuefner@uni-jena.de

nonlocal Fock exchange [20,21]. In this way the well-known problem of a significant underestimation of fundamental gaps by local or semilocal XC functionals is removed [22]. For bulk α-Sn the correct energetic ordering of the Bloch bands at the Γ and L point is achieved [23]. However, the nonlocal exchange treatment significantly increases the computational cost. Computations with more than 80 atoms are not possible. Therefore, for film thicknesses larger than 32 nm, we apply an empirical sp^3s^* tight-binding (TB) model whose parameters are adjusted to reproduce the HSE06 bulk band structure. Thereby, in contrast to previous TB calculations [23] not only intra-atomic SOC is studied. Rather, also matrix elements of the SOC operator between nearest-neighbor atoms [24] are taken into account for a suitable description of the SOC effects on the TSSs. The electronic structure methods and the surface modeling are described in Sec. II. In the two following Secs. III and IV, we present and discuss results for thin and thick α-Sn films. Special care is taken for the dependence on layer thickness and strain as well as the interpretation of the surface states in terms of the bulk electronic structure. Finally, a summary and conclusions are given in Sec. V.

II. METHODS AND MODELING

A. First-principles methods

We apply the DFT within the LDA as implemented in the Vienna *ab initio* simulation package (VASP) [25,26]. The XC functional is parametrized by Perdew and Zunger [27]. Spin-orbit interaction is fully taken into account [28]. Besides the use of the Kohn-Sham eigenvalues of the DFT-LDA [29], band structure calculations are also performed using the hybrid XC functional HSE06 [20,21]. The results of both methods for the band structure of bulk diamond α-Sn are described in detail elsewhere [23]. Within the HSE + SOC approach the energetic ordering of the $p_{3/2}$-derived Γ_8^+, $s_{1/2}$-derived Γ_7^-, and $p_{1/2}$-derived Γ_7^+ bands [30], using the double-group notation, [11,31] and the level distances $-E_g = \Gamma_8^+ - \Gamma_7^- = 0.52$ eV and $\Delta_{\mathrm{SO}} = \Gamma_8^+ - \Gamma_7^+ = 0.68$ eV are in agreement with recent quasiparticle calculations [32]. Here, we apply the slightly different notation Γ_7^- instead of Γ_{6c} (as used for HgTe, see Ref. [23]), since we are not interested in a unified discussion of diamond-structure and zinc-blende-structure zero gap semiconductors. In DFT-LDA the band ordering $\Gamma_7^- < \Gamma_7^+ < \Gamma_8^+$ with level distances $\Gamma_8^+ - \Gamma_7^- = 1.05$ eV and $\Gamma_8^+ - \Gamma_7^+ = 0.69$ eV occurs. Moreover, the L_6^- conduction band minima tend to be below the Fermi level. However, independent of the band ordering the parity eigenvalues of the four valence bands of gray tin at the eight time-reversal invariant momenta (1Γ, $3X$, $4L$) indicate the topological character of the material applying the Fu-Kane theory [33]. Together with the strain-induced gap opening and the strong SOC effects properties of a topological insulator are expected [34].

The electron-ion interaction is described by pseudopotentials that are generated within the projector-augmented wave (PAW) method [35]. The Sn $5s$ and $5p$ electrons are treated as valence electrons. The Sn $4d$ electrons have no major impact on the electronic structure. All calculations are performed including scalar-relativistic effects and SOC [28]. The electronic states in-between the PAW spheres are expanded into a plane-wave basis set with an energy cutoff of 300 eV. In the case of unstrained but also strained α-Sn bulk, the BZ integrations are replaced by a sum over $12 \times 12 \times 12$ Monkhorst-Pack (MP) **k** points [36]. The total energy minimization results into a lattice constant $a_0 = 6.4746$ Å, which is in excellent agreement with measured values [37,38]. The lattice constants of possible nearly lattice-matched zinc-blende substrates, $a_0 = 6.460$ Å (CdTe) and $a_0 = 6.464$ Å (InSb), deviate only slightly, at least in the latter case, from the experimental values [39] due to the applied XC approximation. Both substrates, CdTe(001) and InSb(001), lead to slightly compressively biaxially strained films of α-Sn. Using the calculated lattice constants the lattice misfits amount to -0.23 and -0.16 %. Despite the fact that the experimental observation of TSSs has been made for α-Sn films on InSb [14,15] we study a biaxial strain caused by a CdTe(001) substrate here. However, we will show that the actual compressive biaxial strain is of minor importance.

B. Tight-binding approach

The *ab initio* treatment of the slabs is restricted to about 40 monolayers (ML) of atoms. In order to also treat the electronic structure of slab systems up to 200 atomic layers or more we use an empirical TB model including SOC. Existing TB parametrizations are not sufficiently accurate to reproduce the HSE + SOC band structure. Moreover, the SOC has to be taken into consideration within a better approach than the usual description by an intra-atomic constant to reproduce the splitting $\Delta_{SO} = \Gamma_8^+ - \Gamma_7^+$ of the valence bands at Γ [24]. Parametrization of three-center integrals may improve the fit to a bulk band structure [40]. However, in the case of surface calculations they are difficult to interpret and to be described for the surface atomic layers. These are the reasons why we make minor improvements of the parametrization within a nearest-neighbor approach and an sp^3s^* basis set with a total number of 10 orbitals per atom including spin [23]. Three-center integrals are neglected but, in addition interatomic SOC terms, which give rise to wave-vector-induced Rashba and Dresselhaus band splittings [41,42], are taken into account. The TB parameters are listed in Table I of the Supplemental Material [32]. The HSE06+SOC band structure in Fig. S1, more precisely, 14 of its eigenvalues at the high-symmetry points, five at Γ, three at X, and six at L, are used to fit the first-nearest neighbor parameters. The spin-orbit interaction is described by one intra-atomic parameter and four interatomic

TABLE I. Bulk contributions to slab band states 1–5 (see Fig. 8). The overlap integrals of slab states at Γ and bulk states at Γ, X, or L are given. Each overlap integral is normalized to 100. The irreducible representations are ordered according to their bulk energies with respect to the Fermi level. A slab of 160 ML is studied.

Band label	Energy (eV)	L_6^-	$L_{4,5}^-$	L_6^+	Γ_7^+	Γ_7^-	Γ_8^+	Γ_8^+	X_5	X_5
1	0.019	9	35	1				82	9	1
2	0.000	10	31	1			75	14	1	
3	−0.325	3	4	0	3		10		2	0
4	−0.328			6		13				
5	−0.516			25		57				

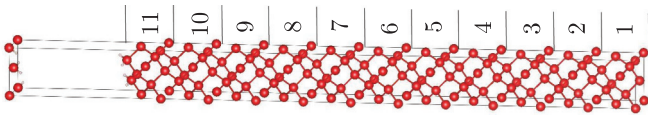

FIG. 1. (Color online) Rectangular slab with (001)$\sqrt{2} \times \sqrt{2}$ surfaces consisting of 44 atomic layers of α-Sn biaxially strained in surface normal direction and a vacuum region with a thickness corresponding to 10 atomic layers. The tin atoms are indicated by large red circles, while the passivating hydrogen atoms are represented by white dots. The labels indicate the 11 irreducible (001) slabs consisting of four atomic layers forming the strained α-Sn material slab.

ones. They represent a generalization of previous choices of the interatomic SOC parameters [24,43] and do not violate the symmetry requirements. In particular, their combination leads to the correct **k**-induced splittings of the uppermost valence bands of the diamond structure. The four parameters in Table I [32] guarantee the correct splittings of the valence bands [41], especially the twofold splitting of the Γ_8^+ band along the [110] direction, in contrast to the fourfold splitting expected for zinc-blende geometry. In order to simulate the biaxially strained bulk material and the surface geometries we apply the Slater-Koster representation of the interatomic TB matrix elements [44] and their d^{-2} scaling with d as the distance between adjacent neighbors [45]. For the description of the hydrogen passivation of the α-Sn(001) surfaces, we use a basis of one hydrogen s orbital and the Sn sp^3s^* hybrid orbitals but neglect ss^* interactions [23].

C. Surface modeling

The α-Sn(001) surface is modeled within the repeated slab approximation. Only symmetric slabs consisting of N irreducible (001) slabs with four atomic layers, i.e., of $4N$ atomic layers in total, are taken into account (see Fig. 1). Each of the layers is biaxially strained according to the lattice mismatch to the zinc-blende substrate, on which an α-Sn film of varying thickness is assumed to be pseudomorphically grown. Such gray tin films can be indeed grown by molecular beam epitaxy on CdTe(001) wafers [46,47]. The strain value -0.23% is used in the theoretical studies. Because of the elastic properties of α-Sn this biaxial strain induces an increase of the layer distances in [001] direction by 0.19%. Calculating the biaxial module $R_b = -2C_{12}/C_{11} = -0.85$ from the elastic constants [48] this increase is understandable. Consequently a tetragonal crystal structure with characteristic atomic distances close to those of the unstrained diamond crystal appears. For the purpose of comparison, results for vanishing strain are also presented.

The (001) surface exhibits two half-filled dangling bonds per surface Sn atom. They may give rise to a 2×1 reconstruction with resulting dimer-derived bands near the Fermi level [49]. Here, we passivate each dangling bond by one hydrogen atom in the direction of the dangling bond. In principle, a 1×1 surface could be studied. However, since the clean surface or the surface passivation by Bi [15] leads to a 2×2 reconstruction, here we study also larger surface unit cells. To simplify the symmetry considerations we investigate square $\sqrt{2} \times \sqrt{2}$ unit cells with two surface Sn atoms and four passivating hydrogen atoms (see Fig. 1). The basis vectors of the two-dimensional (2D) Bravais lattice point along the cubic axes [100] and [010]. Since no **k** dispersion of the bands of the repeated slab system in normal direction is expected and a larger lateral unit cell is used than the primitive one, we apply a $6 \times 6 \times 1$ MP mesh to perform the BZ integration.

III. THIN α-Sn FILMS

We first study relatively small thicknesses of the strained α-Sn films [15], so that an influence of confinement of electrons is likely. With bulk effective masses of 0.0236 m (electrons) or 0.195 m (holes) [39] still large confinement energies of about 159 meV and 19 meV, respectively, can be expected for a thickness of about 100 Å, i.e., for 60 ML. The slab band structure of α-Sn(001)$\sqrt{2} \times \sqrt{2}$ around the Fermi level and the BZ center is displayed in Fig. 2 for 0.23% compressive biaxial strain, hydrogen-passivated surfaces, and a slab thickness of 22 ML. In order to have a chance to depict Dirac cones, for which a high **k**-point density is required, we present Kohn-Sham results obtained within DFT-LDA + SOC in Fig. 2. The difficulties with the DFT-LDA band structure may hardly influence the presented results, as no L point is folded onto the Γ point of the surface BZ. Moreover, the wrong ordering of the Γ_7^- and Γ_7^+ bands does not play an important role, since only the $s_{1/2}$-derived Γ_7^- band is shifted to too low energies by about 0.5 eV [23] and only energies of the order

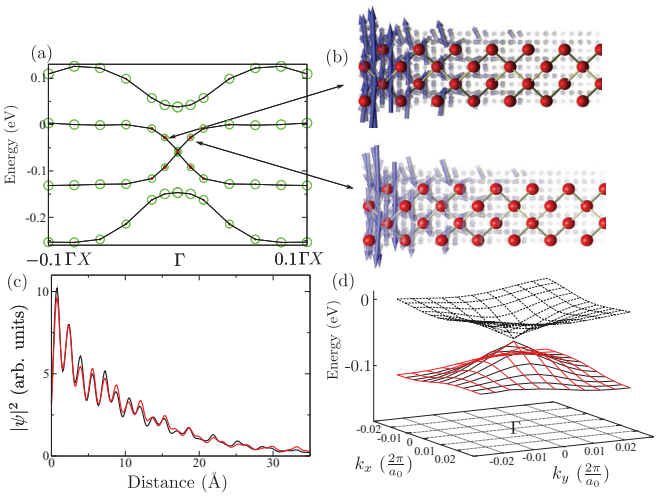

FIG. 2. (Color online) (a) Slab band structure of 0.23% biaxially strained α-Sn with H-passivated surfaces and a thickness of 44 ML within the DFT-LDA approach. The projections onto atomic s (p) orbitals are indicated by the size of red (green) circles. The Fermi level is used as energy zero. (b) Local magnetization density due to the linear band states near Γ. The Sn atoms are shown as red dots. The local spin orientation is indicated by arrows. (c) Wave function square of the band states that are crossing at E_D averaged over planes perpendicular to the surface normal versus distance. The state belonging to the lower cone is depicted in red while the black line indicates the upper one. The position of the uppermost Sn layer is identified with the surface position. (d) Three-dimensional view of the two bands around the Dirac point.

of −0.1 eV below the Fermi energy are studied. Therefore, DFT-LDA + SOC may serve as a first approach to discuss the TSSs. First of all, in agreement with the predictions based on general grounds as number of band inversions, insulating properties, and strong SOC Fig. 2(a) exhibits crossing linear bands near Γ at an energy $E_D = -0.05$ eV, the Dirac point, below the Fermi level. However, both linear bands around Γ are occupied. Another peculiarity is that the atomic character of the band states is not purely p-like as expected, if these bands would be derived from Γ_8^+ bulk bands. Rather, about 30% s contributions are found despite the rather low-lying Γ_7^- band. The s contributions are in agreement with the experimental findings that a TSS emerges out of the s-like Γ_7^- valence bands [14].

Despite these two peculiarities Figs. 2(b) and 2(C) demonstrate the topological character of the linear band states. They are localized near the slab surfaces. Apart from atomic oscillations in Fig. 2(c) the envelope shows a localization near the surface and an exponential decay into the bulk region of the slab with a decay constant of about 10.1 Å. As a consequence the overlap of envelope functions belonging to opposite surfaces of the slab with 40 ML is negligibly small. The spin polarization of the TSSs and their helical character are clearly visible from Fig. 2(b). The linear band states are spin polarized inside the plane perpendicular to the surface normal. For a given wave vector the spin polarizations of the upper and lower Dirac cones [see Fig. 2(d)] are opposite to each other. In each cone there is a rotation of the local (in **k** space) magnetization by comparing the opposite directions ΓX and $-X\Gamma$ with $\Gamma X || [100]$.

If the Fermi level would be moved down to the Dirac point E_D, by doping or a gate voltage, this obvious helicity would give rise to spin channels in which electrons with different spin travel in opposite directions, which may lead to a QSH effect. Indeed, experimental studies [14] show that the Fermi level can be shifted toward the Dirac point for high doping of α-Sn with up to 16% Te atoms. On the other hand, we have to state clearly that the TSSs [Fig. 2(a)] and the resulting Dirac cones [Fig. 2(d)] are below the Fermi level, which contradicts the original definition of a topological insulator where protected metallic surface or edge states cross inside the fundamental gap [1,7,8,34,50,51]. Only with additional manipulations of the energy scale, e.g., by a Fermi level shift, strained α-Sn would fulfill the original definition of a TI.

Figure 2(d) indicates that in the vicinity of Γ the linear bands of TSSs form Dirac cones with $E_D = 0.05$ eV below the Fermi level. The position of the Dirac point below the Fermi level agrees roughly with the experimental findings [14,15]. The corresponding Fermi velocities amount to 0.46 (upper cone) and 0.41 (lower cone) $\times 10^6$ m/s, very close to the DFT-LDA values of the buckled 2D honeycomb crystals silicene and germanene [52]. The calculated values are embedded by the value 0.29×10^6 m/s of a typical 3D TI [53] and 1.0×10^6 m/s of a flat 2D honeycomb crystal such as graphene [54].

The shortcomings of the DFT-LDA approach are removed from theory, applying the nonlocal hybrid HSE06 XC functional and hence quasiparticle corrections in a poor man's way. Results for the largest studied slabs with 40 ML are depicted in Fig. 3. The bands in Fig. 3(a) show similarities but also discrepancies to the DFT-LDA findings in Fig. 2(a).

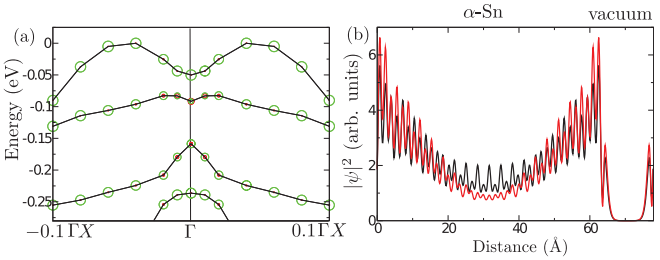

FIG. 3. (Color online) (a) HSE06 band structure of 0.23% compressively strained α-Sn(001)$\sqrt{2} \times \sqrt{2}$ slabs consisting of 40 ML. The s and p character of the states is illustrated by red or green dots of varying size. The energy zero corresponds to the Fermi level. (b) The averaged square of the wave functions of the two TSSs near Γ in the entire unit cell with two surfaces between material slab and vacuum.

In particular, the band dispersion is modified. It is increased for the two bands embedding the Dirac cones in Fig. 2(a). The more pronounced camel-back structure of the highest occupied slab band seems to be a consequence of a stronger SOC due to the localization tendency of the atomic states including 25% Fock-like exchange within the HSE approach. A gap between the upper and lower Dirac cones is opened and gives rise to a significant reduction of the linear band character for the upper Dirac cone. The main reason is illustrated by the spatial variation of the TSS near Γ. It still shows the atomic oscillations, but the exponential decay of its envelope into the slab center is much weaker with a decay constant of about 23 Å compared to the DFT-LDA value. This result is hardly understandable because the nonlocal exchange usually tends to stronger localization of atomic orbitals. It cannot be a consequence of the increased surface barrier within HSE06 [55]. For a nontopological surface state a larger barrier increases the localization of such a state [49]. In any case, the overlap of the TSSs of the two surfaces in the slab center gives rise to a level splitting into a bonding and antibonding combination of the two TSSs and, hence, a gap opening visible in Fig. 3(b). The Dirac point is shifted toward $E_D = -0.15$ eV. The shrinkage of the gap between the Dirac cones for increasing slab thickness has been checked. Our findings are in agreement with the scenario of strong interference between the top and the bottom surface states for very thin films [15]. Differences in the characteristic thicknesses may be due to the fact that the experimentally studied films possess different surfaces, more precisely interfaces between α-Sn and vacuum and α-Sn and InSb, which may give rise to different decay constants for the corresponding envelopes.

IV. THICK α-Sn FILMS

A. Topological character

In order to avoid a gap opening between Dirac cones due to the finite size of the films we have also studied slabs up to a thickness of 184 ML, i.e., of about 300 Å. This is however not anymore possible within the framework of a generalized DFT scheme with a hybrid XC functional such as HSE06. We therefore apply the developed TB scheme (see Sec. II A and Ref. [32]). The electronic structure of α-Sn

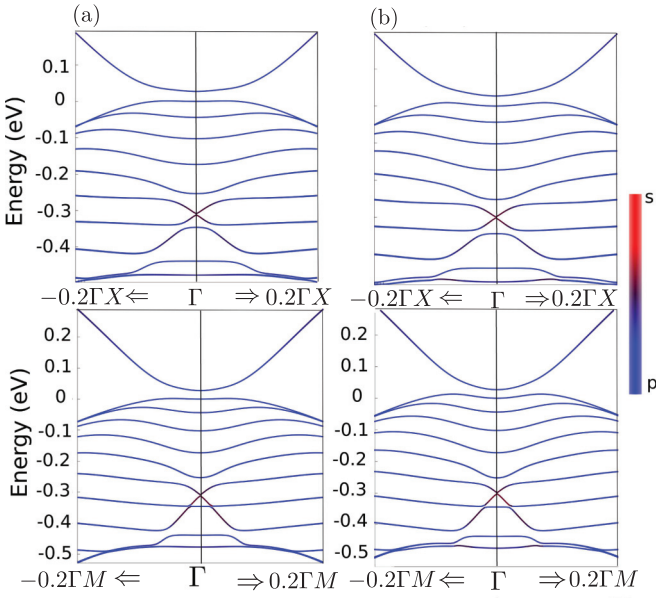

FIG. 4. (Color online) Band structure of repeated α-Sn slabs of 84 ML thickness along two high-symmetry directions $\Gamma X \parallel [100]$ and $\Gamma M \parallel [110]$ in the $(001)\sqrt{2} \times \sqrt{2}$ surface BZ obtained within the framework of the TB method. (a) 0.23% biaxially strained, (b) unstrained. The *s* and *p* character of the underlying states is illustrated by red and blue colors, respectively. The Fermi level defines the energy zero.

slabs with 84 ML is presented in Fig. 4 for two different high-symmetry directions in the surface BZ but strained as well as unstrained material. Conical linear bands are clearly visible independent of the **k** orientation with a Dirac point at an energy of $E_D = -0.3$ eV. The resulting cones (see also Fig. 5) are fully occupied in agreement with the results for thin films in Sec. III and experimental data for undoped samples [14,15]. The extent of the lower cone around the Γ point is however

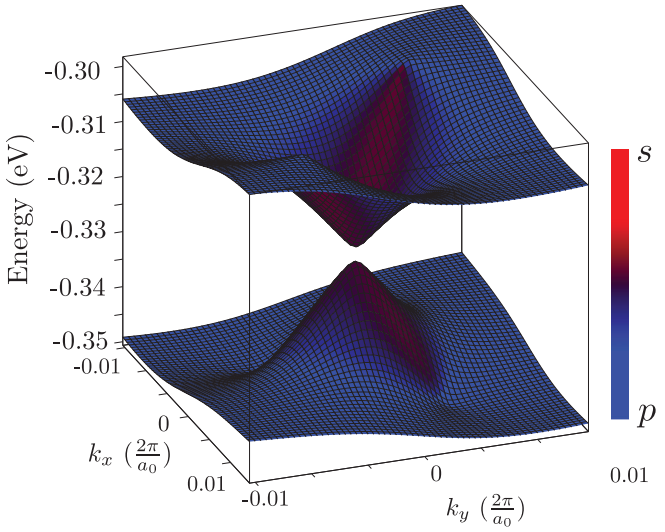

FIG. 5. (Color online) 3D view on the Dirac cones of the α-Sn surface shown in Fig. 4(a) for strained 160 ML slabs. The surface color indicates the contributions of atomic orbitals.

seemingly reduced. This feature will be discussed in detail below. A projection of the linear band states onto atomic orbitals confirms the surprisingly strong *s* character predicted by *ab initio* methods and measurements [14]. The 3D view of the Dirac cones in Fig. 5 indicates a rather isotropic behavior and the fact that the *s* character is strongest near E_D.

However, Fig. 4 also indicates three other features: (i) The slab band structure is hardly affected by the biaxial strain. (ii) The passivated thick films are insulators with the Fermi level in an extremely small gap of the order of 30 meV. Just like the fact that E_D is below the Fermi energy these two features clearly indicate deviations from the picture that strained α-Sn is a conventional TI. (iii) The linearity of the TSS-derived bands is distributed over more bands than the two ones actually crossing at the Dirac point. Energetically close bands develop a linear dispersion continuing the Dirac-cone shape into the Brillouin zone away from Γ. This effect is more pronounced for the lower cone in the [110] direction (lower panels in Fig. 4) compared to the [100] one. The three bands below E_D significantly change their dispersion in the vicinity of Γ toward a cone line shape. This will be discussed in more detail, in particular the thickness dependence of this effect, in the Supplemental Material [32]. The appearance of many slab bands between the Fermi level position and E_D is also illustrated there.

The topological character of the states near E_D is further illustrated in Figs. 6 and 7. The wave function squares of six (twofold degenerate) states at Γ around $E_D = -0.33$ eV

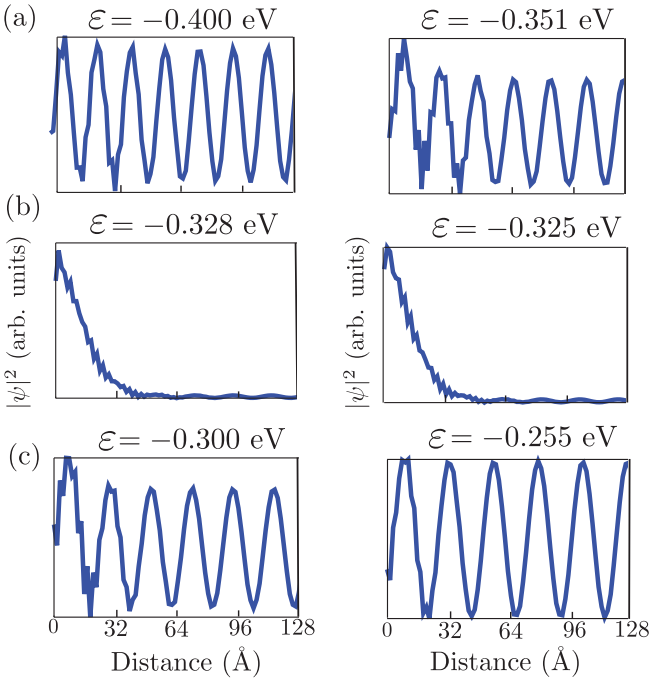

FIG. 6. (Color online) Envelope functions for states near Γ around E_D as obtained from the eigenvectors of the TB theory for a slab of slightly strained 160 ML versus the coordinate along the surface normal. Only one surface, i.e., one half of the slab, is considered. The energies of the six band states are given with respect to the Fermi level. The (a) upper (c) lower panels show states below (above) the topological ones in (b).

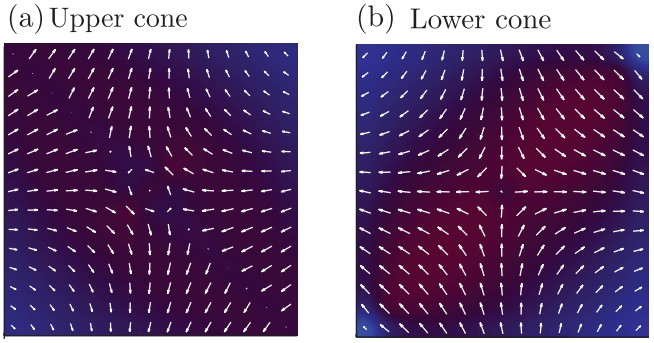

FIG. 7. (Color online) The spin polarization of the upper (lower) Dirac cone for the bands given in Fig. S3 for slabs with 160 ML. The center of each panel is chosen at the Γ point. The edge lengths are $0.02\frac{\pi}{a_0}$. The color scheme of the background is the same as used in Fig. 5 and indicates the atomic orbital character of the band states.

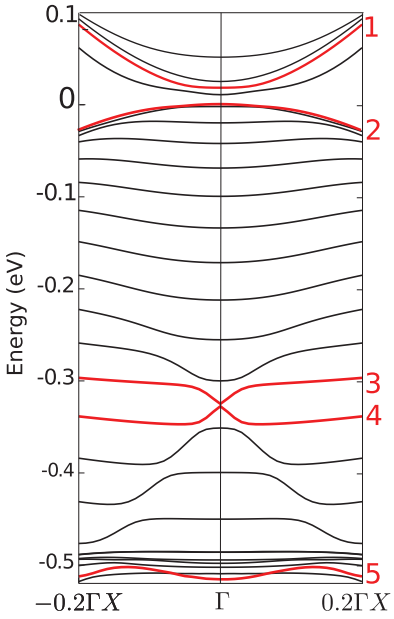

FIG. 8. (Color online) Band structure of the (001) surface of α-Sn within the TB method. The band states which show a strong overlap with bulk states at high-symmetry points or a TSS character are indicated by red lines. The labels 1,. . ., 5 are used in Table I.

have been examined. Two topological edge states separated by 3 meV which are embedded by projected bulk states are identified. The TSSs are localized within about 25 atomic layers below each surface and rapidly decay into the bulk regions in qualitative agreement with the results of the *ab initio* studies in Sec. III. The decay constant amounts to 9 Å. Despite the hydrogen passivation of the surfaces, edge states appear near the slab surfaces. They are obviously protected against surface modifications. Since for the studied slab thickness their overlap vanishes, only a negligible gap occurs near the Dirac point. In order to demonstrate the protection of states we have additionally modeled the surface by a bond cutting method [49], i.e., by shifting the energies of the dangling bonds to infinity. The energies and the wave functions of the TSSs are practically not influenced by the modified boundaries.

Another strong indication for the topological character of states with energies of about E_D is their spin polarization (see Fig. 7). We evaluated the spin polarization as the expectation value of the spin operator with the resulting two-component Pauli spinors. The results for the TSSs are represented in Fig. 7. The direction of the spin polarization varies only inside the surface plane and has no component perpendicular to the surface. The spin is rotated by 2π along a circular isoenergy line around Γ of both lower and upper Dirac cones, confirming their helical character. For opposite directions in the BZ $\mathbf{k} \rightarrow -\mathbf{k}$, the spin orientation is inverted. These results are in formal accordance to the classification of strained α-Sn as strong TI with one Dirac point localized at Γ by Fu and Kane [33]. Considering only the TSS localized at one slab surface the upper and lower cones show opposite spin polarization. This fact is in agreement with the *ab initio* results in Fig. 2(b) and experimental findings [15].

B. Thickness dependence and observability of TSSs

A complete interpretation of the electronic structure results asks for a more detailed analysis of slab, bulk-derived, and topological states. As an example the band structure of a thick strained α-Sn slab with a thickness of 160 ML is displayed in Fig. 8. The insulating character of this slab is clearly visible. The Fermi energy lies in the fundamental gap. The Dirac point and the Dirac cones are clearly visible at and around −0.33 eV.

However, the linear character of these bands near Γ seems to be distributed over adjacent slab bands for larger wave vectors. This fact will be discussed below in more detail. In addition, it is obvious that 11 twofold-degenerate occupied slab bands occur between the upper TSS band near E_D and the Fermi level. In order to better understand the symmetry and the origin of the subband states we have studied the overlap integrals of slab band states and bulk states at Γ, X, and L points. We found substantial bulk contributions only for the five red bands labeled by 1–5 in Fig. 8. The relative values of the overlap integrals are listed in Table I. Thereby, the contribution of the irreducible representations of Bloch states at X is vanishing in agreement with the large energetic distances of 1 or 3 eV of these states to the Fermi level (see Fig. 2 in Ref. [23]). Despite their also relatively large energetic distance the uppermost L valence bands contribute to the two slab bands around the Fermi level. Interestingly the lowest "bulk-like" band is mainly derived from s-like Γ_7^- states but also shows some admixture of L_6^+ states. The two topological states 3 and 4 forming the apex of the Dirac cones near $E_D = -0.33$ eV exhibit bulk contributions. However, they are significantly lower in energy in comparison to the three other states. The gap of the slab system is mainly formed by light-hole Γ_8^+ and heavy-hole Γ_8^+ states. Of course, the situation is not completely understood due to the additional slab band in the gap close to the lowest conduction band. This result again indicates deviations from the conventional picture of a 3D topological insulator for strained α-Sn. The TSSs do not appear between the splitted Γ_8^+ states, rather between the heavy-hole-like Γ_8^+ and the Γ_7^- states in almost agreement with the interpretation of the experimental results [14,15]. Moreover, in Fig. 4(b) it is demonstrated that

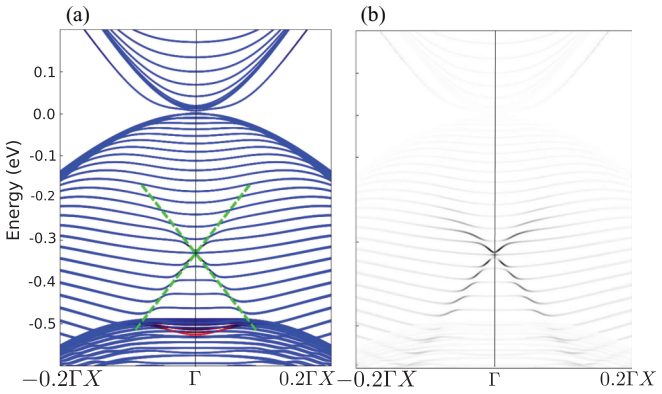

FIG. 9. (Color online) (a) Band structure (blue lines) of a 244 ML slab of strained α-Sn around Γ. The Fermi level is used as energy zero. The blue lines essentially represent p-derived states, whereas the red line indicates s-derived states. The green dashed lines guide the eyes to identify the pieces of the TSS-derived bands with linear wave-vector dispersion. (b) Projection of the band states onto atoms in layers parallel to the surface. The darkness indicates that the corresponding states possess a large probability to find them closer to the surface, whereas subbands belonging to states more located in the bulk-like region of the slab are practically not visible anymore.

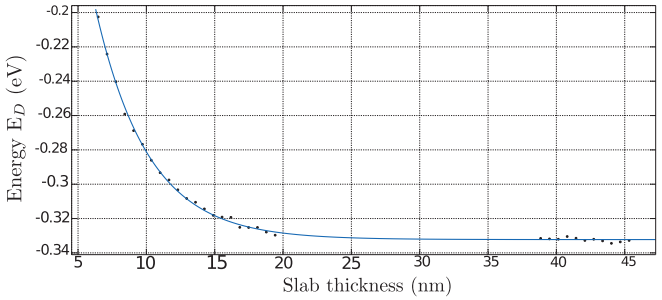

FIG. 10. (Color online) Position of the Dirac point E_D with respect to the Fermi level versus slab size. The blue line describes an exponential fit.

the strain-induced Γ_8 gap is not necessary for the formation of the TSSs.

The question arises how our findings relate to the observation of Dirac cones with a Dirac point below the Fermi level and a lower cone in an energy interval up to -0.6 eV by means of ARPES [14,15]. For that reason we study the slab band structure of a thick 244 ML slab in a wider range of **k** points around the Γ point of the surface BZ and a slightly larger energy region in Fig. 9. First of all, in Fig. 9(a) the high density of slab bands with a minimum or maximum near the Fermi energy and low-lying bands with a camel-back-like dispersion near -0.5 eV is prominent. The upper bands around the Fermi level look very much as the two bulk Γ_8^+ bands with opposite dispersion but slightly split by strain. The red part of the lower band can be identified with the bulk Γ_7^- bulk band [23]. Indeed, these bands have been observed for relatively large photon energies, i.e., large escape depths of the photoelectrons [14]. The occupied slab bands in between allow the identification of the Dirac point $E_D = -0.33$ eV and linear subbands around Γ in an extremely small energy interval of the order of 0.05 eV as discussed above. However, in Fig. 9(b) the adjacent upper and lower subbands show piecewise also a linear band dispersion. These pieces seemingly form a much larger Dirac cone, in particular for energies below E_D. The resulting Fermi velocity amounts to $v_F = 0.58 \times 10^6$ m/s which differs somewhat from the value obtained for the two bands that actually cross at E_D but is in good agreement with the *ab initio* and experimental values. In order to demonstrate the topological character of the states leading to the linear segments of the subbands, we have projected all band states to Sn atoms in atomic layers below the surface. We have assumed an exponential weakening with a decay constant of the order of the escape depth of photoelectrons for small photon energies. The layer contributions are displayed in Fig. 9(b) by a decreasing intensity with increasing distance to the surface. The results are qualitatively identical with ARPES results for photon energies of about 20 eV and, hence, for a pronounced surface sensitivity.

Reducing the thickness of the α-Sn slabs we found qualitatively similar results as shown in Figs. 2 and 4 but with a smaller number of slab bands in the same energy regions. Thereby, the linear dispersion is distributed over a smaller number of subbands and is, hence, less visible. Moreover, there is a clear effect on the Dirac point position with respect to the Fermi level. It is illustrated in Fig. 10. It almost shows an exponential behavior with a saturation of the position near $E_D = -0.33$ eV with rising slab thickness. Such a tendency has been observed experimentally by Ohtsubo *et al.* [15] with $E_D = -0.2$ eV for about 30 ML in reasonable agreement with Fig. 10. The corresponding value observed by Barfuss *et al.* [14] is smaller. The discrepancy may be a consequence of band bending appearing in real semiconductor samples grown on InSb(001) substrates which are likely n-type.

V. SUMMARY AND CONCLUSIONS

We have studied the electronic structure of compressively biaxially strained α-Sn slabs of varying thickness by means of *ab initio* and TB methods including spin-orbit interaction. As model surfaces freestanding hydrogen-passivated (001)$\sqrt{2} \times \sqrt{2}$ slabs are investigated. They guarantee the absence of chemical surface states. The slab thicknesses are varied between 24 and 244 monolayers. Usually a biaxial strain of -0.23% is assumed. In some test cases unstrained systems have also been studied.

For not too small film thicknesses we found the formation of upper and lower Dirac cones formed by a pair of helical edge or topological surface states as predicted by model studies in the literature. However, we also found some significant discrepancies to the conventional picture of a 3D topological insulator. First of all the Dirac cones are situated below the Fermi level of undoped and unbiased α-Sn films and not in the Γ_8^+-derived gap opened by the biaxial strain. Rather, for not too small film thicknesses the linear bands appear mainly between heavy-hole-like Γ_8^+ and electron-like Γ_7^- bulk-derived bands in agreement with experimental observations. This means that the TSSs indeed appear inside a bulk gap, but not inside a gap between occupied and unoccupied bands but the negative $\Gamma_8^+ - \Gamma_7^-$ bulk sp band gap. The influence of a strain-induced fundamental gap therefore seems to be negligible. For smaller

slab thicknesses the situation is more complex. A gap between the Dirac cones may be opened due to confinement effects for small slab size. The Dirac cones observed by ARPES under surface-sensitive conditions are explained by pieces of slab subbands with linear dispersion. The resulting Fermi velocity agrees with the measured values.

Since the Dirac points are below the Fermi level, it will be difficult to observe spin currents at the surface and, therefore, a quantum spin Hall phase for as-grown samples. However, a shift of the Fermi level toward larger binding energies by gate voltages, doping or band bending may bring the Dirac point close to it. Such manipulations indicate a promising potential to demonstrate physical effects for α-Sn films of varying thickness and varying Fermi level position.

ACKNOWLEDGMENTS

Valuable scientific discussion with G. Bihlmayer, J. Furthmüller, and J. Schäfer are acknowledged. We gratefully acknowledge financial support from the Austrian Science Fund (FWF) through Special Research Programme F25 (SFB IR-ON).

[1] C. L. Kane and E. J. Mele, Phys. Rev. Lett. **95**, 146802 (2005).
[2] B. A. Bernevig, T. L. Hughes, and S.-C. Zhang, Science **314**, 1757 (2006).
[3] L. Fu, C. L. Kane, and E. J. Mele, Phys. Rev. Lett. **98**, 106803 (2007).
[4] M. König, S. Wiedmann, C. Brüne, A. Roth, H. Buhmann, L. W. Molenkamp, X.-L. Qi, and S.-C. Zhang, Science **318**, 766 (2007).
[5] D. Hsieh, D. Qian, L. Wray, Y. Xia, Y. S. Hor, R. J. Cava, and M. Z. Hasan, Nature (London) **452**, 970 (2008).
[6] D. Hsieh, Y. Xia, D. Qian, L. Wray, J. H. Dil, F. Meier, J. Osterwalder, L. Patthey, J. G. Checkelsky, N. P. Ong, A. V. Fedorov, H. Lin, A. Bansil, D. Grauer, Y. S. Hor, R. J. Cava, and M. Z. Hasan, Nature (London) **460**, 1101 (2009).
[7] J. Moore, Nat. Phys. **5**, 378 (2009).
[8] M. Z. Hasan and C. L. Kane, Rev. Mod. Phys. **82**, 3045 (2010).
[9] S. Murakami, N. Nagaosa, and S.-C. Zhang, Phys. Rev. Lett. **93**, 156804 (2004).
[10] C. Brüne, C. X. Liu, E. G. Novik, E. M. Hankiewicz, H. Buhmann, Y. L. Chen, X. L. Qi, Z. X. Shen, S. C. Zhang, and L. W. Molenkamp, Phys. Rev. Lett. **106**, 126803 (2011).
[11] P. Yu and M. Cardona, *Fundamentals of Semiconductors* (Springer, Berlin, 1996).
[12] D. A. Kozlov, Z. D. Kvon, E. B. Olshanetsky, N. N. Mikhailov, S. A. Dvoretsky, and D. Weiss, Phys. Rev. Lett. **112**, 196801 (2014).
[13] I. Tsidilkovski, *Gapless Semiconductors–a New Class of Materials* (Akademie-Verlag, Berlin, 1988).
[14] A. Barfuss, L. Dudy, M. R. Scholz, H. Roth, P. Höpfner, C. Blumenstein, G. Landolt, J. H. Dil, N. C. Plumb, M. Radovic, A. Bostwick, E. Rotenberg, A. Fleszar, G. Bihlmayer, D. Wortmann, G. Li, W. Hanke, R. Claessen, and J. Schäfer, Phys. Rev. Lett. **111**, 157205 (2013).
[15] Y. Ohtsubo, P. Le Fèvre, F. Bertran, and A. Taleb-Ibrahimi, Phys. Rev. Lett. **111**, 216401 (2013).
[16] G. Cubiotti, Y. Kucherenko, A. Yaresko, A. Perlov, and V. Antonov, J. Phys. Condens. Matter **11**, 2265 (1999).
[17] A. D. Becke, J. Chem. Phys. **98**, 1372 (1993).
[18] F. Tran and P. Blaha, Phys. Rev. Lett. **102**, 226401 (2009).
[19] S. Küfner and F. Bechstedt, Phys. Rev. B **89**, 195312 (2014).
[20] J. Heyd, G. E. Scuseria, and M. Ernzerhof, J. Chem. Phys. **118**, 8207 (2003).
[21] J. Heyd, G. E. Scuseria, and M. Ernzerhof, J. Chem. Phys. **124**, 219906 (2006).
[22] W. G. Aulbur, L. Jönsson, and J. W. Wilkins, Solid State Phys. **54**, 1 (1999).
[23] S. Küfner, J. Furthmüller, L. Matthes, M. Fitzner, and F. Bechstedt, Phys. Rev. B **87**, 235307 (2013).
[24] T. B. Boykin, Phys. Rev. B **57**, 1620 (1998).
[25] G. Kresse and J. Furthmüller, Phys. Rev. B **54**, 11169 (1996).
[26] G. Kresse and J. Furthmüller, Comp. Mater. Sci. **6**, 15 (1996).
[27] J. P. Perdew and A. Zunger, Phys. Rev. B **23**, 5048 (1981).
[28] D. Hobbs, G. Kresse, and J. Hafner, Phys. Rev. B **62**, 11556 (2000).
[29] W. Kohn and L. J. Sham, Phys. Rev. **140**, A1133 (1965).
[30] F. H. Pollak, M. Cardona, C. W. Higginbotham, F. Herman, and J. P. Van Dyke, Phys. Rev. B **2**, 352 (1970).
[31] R. Enderlein and N. J. M. Horing, *Fundamentals of Semiconductor Physics and Devices* (World Scientific Publishing, Singapore, 1997).
[32] See Supplemental Material at http://link.aps.org/supplemental/10.1103/PhysRevB.90.125312 for the electronic structure of unstrained and strained α-Sn.
[33] L. Fu and C. L. Kane, Phys. Rev. B **76**, 045302 (2007).
[34] L. Müchler, H. Zhang, S. Chadov, B. Yan, F. Casper, J. Kübler, S.-C. Zhang, and C. Felser, Angew. Chem. Int. Ed. **51**, 7221 (2012).
[35] G. Kresse and D. Joubert, Phys. Rev. B **59**, 1758 (1999).
[36] H. J. Monkhorst and J. D. Pack, Phys. Rev. B **13**, 5188 (1976).
[37] R. Farrow, D. Robertson, G. Williams, A. Cullis, G. Jones, I. Young, and P. Dennis, J. Cryst. Growth **54**, 507 (1981).
[38] J. Thewlis and A. R. Davey, Nature (London) **174**, 1011 (1954).
[39] W. Martienssen and H. Warlimont, *Springer Handbook of Condensed Matter and Materials Data*, Bd. 1 (Springer, Berlin, 2005).
[40] Y. Li and P. J. Lin-Chung, Phys. Rev. B **27**, 3465 (1983).
[41] G. Dresselhaus, Phys. Rev. **100**, 580 (1955).
[42] Y. A. Bychkov and E. I. Rashba, J. Phys. C **17**, 6039 (1984).
[43] See AIP Document No. E.PAPS.E-PRBMDO-57-1627 for the relationships between nearest-neighbor spin-orbit parameters in diamond. http://www.aip.org/epaps/epaps.html.
[44] J. C. Slater and G. F. Koster, Phys. Rev. **94**, 1498 (1954).
[45] W. Harrison, *Electronic Structure and the Properties of Solids* (Dover, New York, 1989).
[46] J. L. Reno and L. L. Stephenson, J. Electron. Mater. **19**, 549 (1990).
[47] J. A. Gómez, D. Guenzburger, D. E. Ellis, M. Y. Hu, E. Alp, E. M. Baggio-Saitovitch, E. C. Passamani, J. B. Ketterson, and S. Cho, Phys. Rev. B **67**, 115340 (2003).
[48] O. Madelung, *Semiconductors: Group IV Elements and III-V Compounds* (Springer-Verlag, Berlin, 1991).

[49] F. Bechstedt, *Principles of Surface Physics* (Springer-Verlag, Berlin, 2003).
[50] X.-L. Qi and S.-C. Zhang, Rev. Mod. Phys. **83**, 1057 (2011).
[51] Y. Ando, J. Phys. Soc. Jpn. **82**, 102001 (2013).
[52] L. Matthes, P. Gori, O. Pulci, and F. Bechstedt, Phys. Rev. B **87**, 035438 (2013).
[53] K. Kuroda, M. Ye, A. Kimura, S. V. Eremeev, E. E. Krasovskii, E. V. Chulkov, Y. Ueda, K. Miyamoto, T. Okuda, K. Shimada, H. Namatame, and M. Taniguchi, Phys. Rev. Lett. **105**, 146801 (2010).
[54] C. Berger, Z. Song, X. Li, X. Wu, N. Brown, C. Naud, D. Mayou, T. Li, J. Hass, A. N. Marchenkov, E. H. Conrad, P. N. First, and W. A. de Heer, Science **312**, 1191 (2006).
[55] B. Höffling, A. Schleife, C. Rödl, and F. Bechstedt, Phys. Rev. B **85**, 035305 (2012).